Penetration Characteristics of a Liquid Droplet Impacting on a Narrow Gap: Experimental and Numerical Analysis

D. J. Bouchard[*1], M. Andredaki[2], A. Georgoulas[2], M. Marengo[2], S. Chandra[1]

[1]Department of Mechanical and Industrial Engineering, University of Toronto, Toronto, M5S 3G8, Canada
*Corresponding author: jordan.bouchard@mail.utoronto.ca

[2]Advanced Engineering Centre, School of Architecture Technology and Engineering, University of Brighton, Brighton, BN2 4GJ, U.K.

Abstract

Experimentalists are limited in the amount of information they can derive from drop impact experiments on porous surfaces because of the short timescales involved and the normally opaque nature of porous materials. Numerical simulations can supplement experiments and provide researchers with previously unattainable information such as velocity and pressure profiles, and quantification of fluid volume flow rates into the pores. Ethanol drops, 2.0 mm in diameter, are impacted on a narrow gap at Weber numbers that match the impact of water drops, also 2.0 mm in diameter, on the same gap size in a previous study. The experiments show the ethanol drops cleaving at all Weber numbers tested, while the water drops completely enter the gap at low Weber numbers and only cleave at higher Weber numbers. A Volume Of Fluid numerical model of the experiments is constructed in OpenFOAM and used to probe the interior of the drops during impact. For the water drop, a high-pressure region fills the drop during impact which continuously drives liquid into the gap. For the ethanol drops, the high-pressure region is smaller and quickly attenuates, which results in a near-zero vertical velocity at the entrance of the gap. Compared to water, the lower surface tension of ethanol causes these drops to spread further upon impact, recoil less, and overall have less liquid over the gap, which promotes cleaving. Against a superficial thought, when the penetration of liquids into porous materials is to be maximized, a higher surface tension liquid is therefore desirable.

Keywords

Droplet penetration, Droplet impact, Porous substrate, Experimental measurements, Numerical modelling, Volume Of Fluid, OpenFOAM

1. Introduction

The behaviour of drops, both sessile and impacting at some velocity, on surfaces has been studied extensively by various groups worldwide. This multi-decade undertaking is justified because it brings improved control and process improvements to the many industries that utilize drops or sprays in their operations: pharmaceutical, agribusiness, printing, painting and coatings, chemical processing, thermal management, medical applications and several more. Many of the significant findings and advances have been recently reviewed for solid surfaces [1,2] granular media [3], porous layers [4], and when heat transfer is involved [5]. The area that we are interested in understanding further is drop impact on complex surfaces. Some examples of complex surfaces are meshes and wires; surfaces with microstructures, gaps, or holes; or a porous material. This is relevant in the context of the world's most recent pandemic where respiratory droplets would impact the smaller fibres and openings of a woven mask. Studying drop impact on porous materials is challenging because they are normally opaque, and we have limited means to visualize the drop infiltrating inside of them, especially in the milliseconds following droplet impact. Despite this challenge, good progress has been made in understanding how porous materials, in particular, influence drop impact dynamics.

Lee et al. [6,7] impacted water drops on porous stones while tracking the volume of water on the surface of the stones with high-speed photography and employing neutron radiography to measure the amount of water that infiltrated into the stones over time. Higher impact velocities lead to shorter droplet infiltration times because faster travelling drops tend to spread and pin further on the surface than slower travelling drops. This larger drawing area leads to faster infiltration. The region inside the stones that becomes saturated with water is affected by the impact velocity as well. Low velocity impacts tend to be semi-spherical in shape; high velocity impacts tend to spread out wider below the surface—the radius of the wetted region is more sensitive to the impact velocity than the depth. The semi-spherical shapes of the saturated porous material agree with earlier findings by Reis et al. [8] on beds of glass beads and sand which had greater pore sizes and porosity.

One point of controversy in the literature of drop impact on porous surfaces is how much liquid from the drop is driven into the porous material from the time of impact until the liquid rests on the surface - termed *inertial driven liquid flow*. An example comes from Roisman et al. [9] who found that the splashing threshold can be supressed on porous and rough surfaces, and they suggest that this may be because of liquid being driven into the porous surface, leaving less kinetic energy in the drop spreading on the surface. However, Lee et al. [7] concluded from the analysis of their data that the volume of inertial driven liquid is negligible on their porous stones.

We do not yet know what combination of drop and surface characteristics leads to simultaneous drop infiltration during spreading and under what conditions we can consider the amount of inertial driven liquid negligible. The studies completed so far towards answering this question investigate a drop impacting a single pore so the impact and infiltration of a drop can be observed simultaneously at the millisecond time resolution that is needed.

Delbos et al. [10] impacted water and glycol drops travelling at several velocities onto hydrophobic and hydrophilic capillaries of various internal radii. For hydrophilic capillaries they list three possible outcomes depending on the impact velocity of the drop: total impregnation, the drop is completely wicked into the capillary; the bubbling regime—the drop completely wicks into the capillary but with a trapped air bubble; and the slug formation regime—the drop becomes disconnected from the liquid in the capillary resulting in a large portion of the drop on the top edge of the capillary and a small quantity in the capillary. Balancing the kinetic energy of impact with the viscous dissipation of the liquid on the capillary walls yields a threshold velocity that delineates the total impregnation regime from the bubbling and slug forming regimes. Larger capillary radii and faster travelling drops tend to be in the slug forming regime.

Ding and Theofanous [11] numerically studied the experiment of [10] to analyse aspects that were inaccessible experimentally and to expand the parameter space. The resulting pressure contours of the simulation show that there exists a stagnation circle around the pore that stays relatively fixed in space for the duration of the transient impact period. The radius of the stagnation circle is 30% larger than the radius of the capillary, and most of the liquid in the cylinder within the stagnation circle enters the pore. This forcing of extra liquid into the pore leads to the higher pore fluid velocity that has been observed previously and a slug length longer than the diameter of the drop. They expanded on the conditions required to transition from one regime to the next to include the geometry of the capillary opening, and the contact angle hysteresis of the liquid-gas-solid triple line. Slugs will tend to form around openings with sharp transitions and with liquids that have a larger contact angle hysteresis. A smaller receding contact angle will tend to pin the drop, preventing it from coalescing over the top of the capillary.

Recently, Andredaki et. al [12] numerically expanded the experiments of [10] to investigate quasi-sessile droplet absorption into cylindrical pores as a first step towards understanding, identifying, and quantifying wound exudate absorption into wound dressing capillaries. It is shown that distinct droplet absorption rates exist, described by specific relationships, that can predict the absorption rates for particular values of pore size and liquid viscosity. For the examined dimensionless parameters ranges, these distinct droplet absorption rates are directly linked with four different droplet evolution regimes that are grouped in a well-defined flow map. Finally, it has been also illustrated that the resulting liquid absorption rates are not significantly affected by the initial droplet diameter.

Bouchard and Chandra [13] studied a different single-pore geometry by impacting water drops on a narrow gap—a model for a pore which has one dimension much larger than the diameter of the drop. The entrance into the gap was bevelled instead of the sharp transition of [10]. The velocity of the fluid in the pore was initially higher than the impact velocity, and it was this higher velocity that was used to predict the transition between regimes. They, as in [10], also observed the slug formation regime to coincide with the running out of liquid above the pore. However, unlike Delbos et al. [10], a bubbling regime was not observed for their narrow gap pore geometry.

The present study further expands on the experiments performed in [13] by impacting Anhydrous Ethyl alcohol (ethanol) drops onto a narrow gap—a liquid with a different surface tension but similar viscosity as water. Both sets of experiments are numerically reproduced and analysed to gather data not accessible in the experiments. The main focus is on how the pressure and velocity contours develop within the drop and within the penetrating profile.

Specifically, we identify stagnation regions in the proposed geometry and explain how these contours affect the final volume of liquid in the pore. The shape of the meniscus at the leading edge of the penetrating liquid profile is also investigated. The drop's inertia influences the shape of this meniscus and the initial capillary infiltration dynamics even at low impact velocities (We<7) [13]. For this purpose, an enhanced, user-defined, Volume Of Fluid (VOF) model that has been developed by the authors in OpenFOAM is used. In more detail, the capabilities of the original VOF-based solver of OpenFOAM have been extended by appropriately treating the solver for the dampening of spurious velocities in the vicinity of the interface, a well-known defect of VOF-based methods that in most cases leads to unphysical results, and by the implementation of a more accurate dynamic contact angle model in order to capture correctly the effect of wettability in the simulated cases [14].

2. Materials and Methods

2.1 Experimental Set-up

A narrow parallel gap was created using two uncoated N-BK7 borosilicate glass plates (50 mm x 50 mm x 4 mm) (stock# 47-944; Edmund Optics, Inc. Barrington, NJ, USA). Two 100 μm stainless steel feeler gauges (McMaster-Carr, Aurora, OH, USA) were inserted between the glass plates and then lightly clamped together to maintain a uniform gap spacing. A 2.0 mm diameter Anhydrous Ethyl alcohol (ethanol) drop (1.97 mm, [95%CI: 1.96 mm, 1.98 mm], N= 13) was dropped on the narrow gap at various heights to achieve impact velocities close to 0.04, 0.32, 0.62, and 0.9 m/s. The impact velocities were chosen to match the Weber number of the impacting 2.0 mm water drops in [13]. The measured impact velocities were between -0.02 and +0.05 m/s of the values reported in Table 1; for discussion purposes, the values listed in Table 1 will be used. The experimental measurements were repeated for each impact velocity four times. Glass cleaning methods, high-speed photography, drop deposition, contact angle measurements, and post processing of the images were all performed as previously described in [13]. The scale used to process the images is estimated to be accurate within 2 pixels and the location of the drop's boundary is estimated to be accurate within 2 pixels. The uncertainty in the drop diameter is 2.0±0.08 mm. The uncertainty in the drop's initial

volume is 4.2±0.53 µl. Table 1 lists the experimental conditions used in this study and the measured contact angles for the liquid-solid system. In the previous study where water was used [13], the impact velocities, ordered from least to greatest to correspond to the Weber numbers in Table 1, are: 0.06, 0.5, 1.0, and 1.5 m/s. The measured advancing and receding contact angles for both the edge and face of the glass are indicated in Figure 1 for water and ethanol.

Table 1: Experimental conditions for ethanol drops impacting on a 100 µm gap and contact angles measured for this liquid-solid system.

Liquid-Solid System	Apparent Contact Angles	Impact Velocities [m/s]	Weber Number
borosilicate glass 60-40 surface quality US Standard: MIL-PRF-13803B **ethanol** ρ = 788 kg/m^3 @20°C µ = 1.35 mPas @ 20°C	Edge of glass: θ_A: 22.6°; 95%CI: 19.6°, 25.4°; N=10 θ_R: 1.5°; 95%CI: 0°, 4.3°; N=10 Face of glass: θ_A: 15.8°; 95%CI: 14.8°, 16.8°: N=10 θ_R: 1.3°; 95%CI: 0.4°, 2.3°; N=10	0.04	0.1
		0.32	7.0
		0.62	28.0
		0.9	63.0

2.2 Numerical Simulation Method

An improved VOF based model, which has been previously implemented in OpenFOAM CFD Toolbox (an open source CFD software), is utilised. In more detail, all the numerical simulations of the present work were performed with the finite volume–based CFD code OpenFOAM, using a custom, user-enhanced version of its original VOF-based solver "interFoam".

With the VOF approach, the transport equation for the volume fraction of the liquid phase, α, is solved simultaneously with a single set of continuity and Navier–Stokes equations for the entire flow field. The corresponding volume fraction of the gas phase is simply calculated as $(1-\alpha)$. The main underlying assumptions are that the two fluids are Newtonian, incompressible, and immiscible. The governing equations can be written as,

$$\nabla \cdot \vec{U} = 0 \tag{1}$$

$$\frac{\partial \rho_b \vec{U}}{\partial t} + \nabla \cdot \left(\rho_b \vec{U}\vec{U}\right) = -\nabla p + \nabla \cdot \mu_b \left(\nabla \vec{U} + \nabla U^T\right) + \rho_b f + F_s \tag{2}$$

$$\frac{\partial a}{\partial t} + \nabla \cdot \left(\alpha \vec{U}\right) - \nabla \cdot (\alpha(1-\alpha)U_r) = 0 \tag{3}$$

where the bulk fluid properties (ρ_b, μ_b) are calculated as weighted averages of the liquid (ρ_l, μ_l) and gaseous (ρ_g, μ_g) phase properties as follows,

$$\rho_b = \rho_l \alpha + \rho_g (1-\alpha) \tag{4}$$

$$\mu_b = \mu_l \alpha + \mu_g (1-\alpha) \tag{5}$$

The surface tension force is modelled as a volumetric force using the Continuum Surface Force (CSF) method by Brackbill et al. [15] applying the following equations,

$$F_s = \gamma \kappa (\nabla \alpha) \tag{6}$$

$$\kappa = \nabla \cdot \left(\frac{\nabla \tilde{\alpha}}{|\nabla \tilde{\alpha}|} \right) \tag{7}$$

where, γ is the surface tension coefficient and κ is the curvature of the interface. As mentioned previously, the utilized numerical framework constitutes an enhanced version [16] of the original VOF-based solver of OpenFOAM [17], that suppresses numerical artefacts of the original model, known as "spurious currents". The proposed enhancement involves the calculation of the interface curvature, κ, using the smoothed volume fraction values, $\tilde{\alpha}$, which are obtained from the initially calculated α field, smoothing it over a finite region near the interface. All other equations are using the initially calculated (non-smoothed) volume fraction values of α. Further details on the proposed implementation as well as its validation against experimental measurements can be found in [16].

Furthermore, in order to accurately account for wettability effects, Kistler's Dynamic Contact Angle (DCA) model [18], has been also implemented in the proposed VOF solver which calculates the DCA, θ_d, using the Hoffman function, f_{Hoff}, as follows:

$$\theta_d = f_{Hoff}\left[C_a + f_{Hoff}^{-1}(\theta_\varepsilon) \right] \tag{8}$$

where, θ_ϵ is the equilibrium contact angle. The capillary number, C_a, is calculated with respect to the spreading velocity of the contact line, U_{CL}, and f_{Hoff}^{-1} is the inverse function of "Hoffman's" empirical formulae which is calculated as shown below,

$$f_{Hoff} = acos\left[1 - 2tanh\left(5.16 \left(\frac{x}{1 + 1.31x^{0.99}} \right)^{0.706} \right) \right] \tag{9}$$

where x is equal to:

$$x = f_H \left[Ca + f_H^{-1}\left(\theta_{\mathrm{eq}} \right) \right] \tag{10}$$

The capillary number is defined as,

$$Ca = \frac{\mu U_{CL}}{\gamma} \tag{11}$$

The equilibrium angle, θ_ε, is replaced by either a limiting advancing (θ_A) or receding contact angle (θ_R), depending on the sign of the velocity vector at the contact line. Further details on the development and validation of the proposed DCA implementation can be found in [14].

2.3 Numerical Simulation Set-up

For pressure-velocity coupling, the PISO (Pressure-Implicit with Splitting of Operators) scheme is applied. The transient terms in the equations are discretised using a second order, bounded, implicit scheme (Euler scheme). The calculation time step is controlled by setting the maximum Courant number to 0.2. With this adaptive time-stepping technique, the time step is automatically varied from approximately 10^{-9} to 10^{-6} seconds for the overall simulation cases that are presented in this paper. The gradient terms are discretised using a second-order, Gaussian integration with linear

interpolation (Gauss linear). For the divergence terms, different discretisation schemes are applied for each term in the equations. In more detail, the convection term of Equation (2) is discretised using a "Gauss upwind" scheme. The $\nabla \cdot (\alpha \vec{U})$ term of Equation (3) is discretised using the "Gauss vanLeer" scheme, while the $\nabla \cdot (\alpha(1-\alpha)U_r)$ term is discretised using the "Gauss interfaceCompression" scheme which ensures the boundedness of the calculated volume fraction field. Finally, all Laplacian terms are discretised using the "Gauss Linear Corrected" scheme. Further details on the proposed discretisation schemes can be found in OpenFOAM documentation [17]. It should be mentioned that this was the optimum combination of discretisation schemes in order to maintain a balance between accuracy, convergence and numerical stability during the computations. The proposed numerical set-up has already been largely validated in [12,14,16].

In the present work, four specific cases from the droplet impact experiments reported in [13] are numerically reproduced. Moreover, the four new ethanol experiments that are conducted for the purposes of the present investigation are also reproduced numerically. These experiments were numerically reproduced to give quantitative information that is difficult to obtain from the post-processing and analysis of the experimental measurements as well as to serve as an additional validation study. A schematic of the investigated phenomenon and the considered initial conditions is depicted in Figure 1. A 2.0 mm diameter droplet at ambient conditions impacts a narrow gap that has a width of either 100 or 150 μm for water droplets and 100 μm for ethanol droplets. The impact velocity for the water droplets is either 0.5 or 1.5 m/s while for the ethanol droplets impact velocity values of 0.04, 0.32, 0.62, and 0.90 m/s are used. The horizontal surfaces to the left and right side of the narrow gap, where the spreading of the droplet takes place after the impact, have a wettability that is characterised by an advancing and a receding contact angle of 92.8° and 27.0° for water and 22.5° and 1.5° for ethanol, respectively. The vertical surfaces between the glass plates where the imbibition of the droplet takes place are characterised by an advancing and a receding contact angle of 36.6° and 8.2° for water and 15.8° and 1.3° for ethanol, respectively.

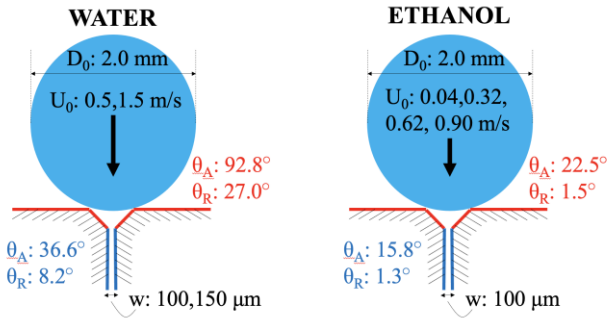

Figure 1. Schematic representation and initial conditions of the investigated phenomenon.

The main initial conditions, the geometric characteristics and the computational grid size for the proposed numerical simulations are summarised in Table 2, while the utilised computational geometry, mesh and boundary conditions are depicted in Figure 2.

Table 2. Initial conditions, geometric characteristics, and computational grid size of numerically reproduced droplet impact cases

	D_0 [mm]	**U_0 [m/s]**	**w [μm]**	**Working Fluid**	**Grid Size [cells]**
Case 1	2.0	0.5	100	water	61,418,900

Case 2	2.0	1.5	100	water	61,418,900
Case 3	2.0	0.5	150	water	61,500,767
Case 4	2.0	1.5	150	water	61,500,767
Case 5	2.0	0.04	100	ethanol	61,418,900
Case 6	2.0	0.32	100	ethanol	61,418,900
Case 7	2.0	0.62	100	ethanol	61,418,900
Case 8	2.0	0.90	100	ethanol	61,418,900

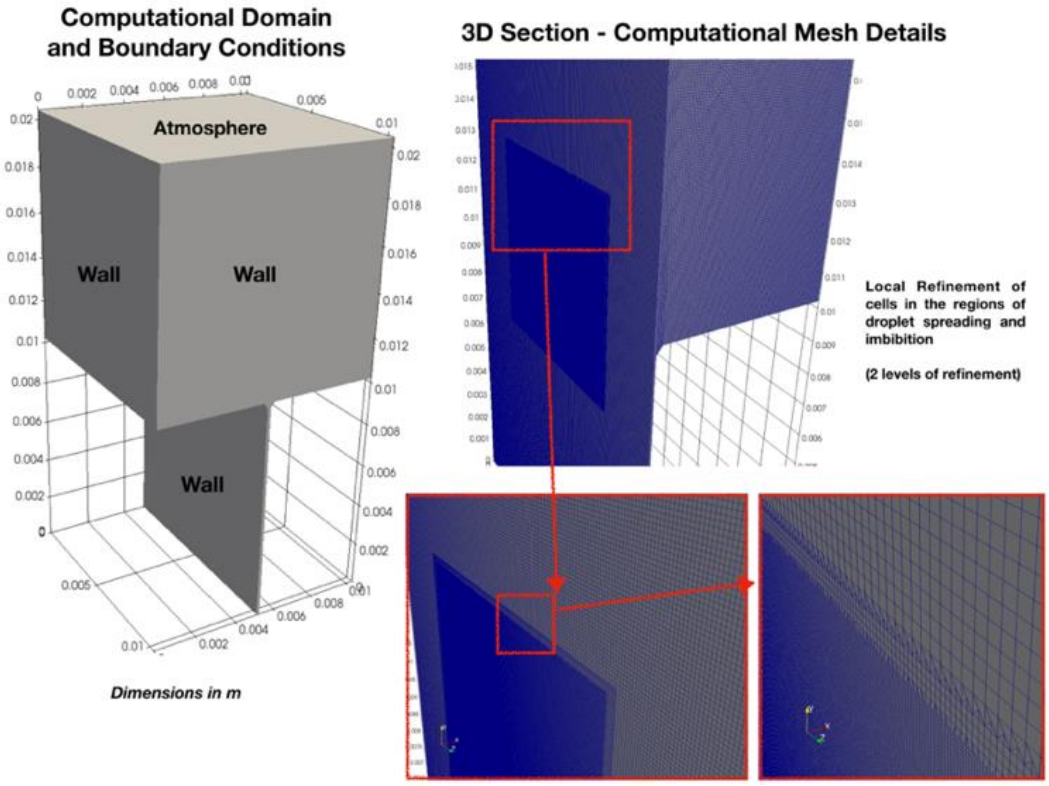

Figure 2. Computational geometry, mesh and boundary conditions.

As can be observed in Figure 2, a 3D, uniform, structured mesh with two successive levels of local grid refinement in the regions of droplet spreading and imbibition is used in each case. The overall size of the computational meshes is 61,418,900 and 61,500,767 cells for the geometries with the 100 μm and 150 μm gap, respectively, and the nominal dimension of the smallest cell is 2 microns. A total of 5 ms after the droplet impact were simulated for the water droplet cases and 15 ms for the ethanol droplet cases. Parallel computations with 600 computational cores in a High-Performance-Computing (HPC) facility were utilised for these simulations. The high number of computational cells is generally needed, in order to adequately capture the imbibition profiles within the narrow gaps as well as to have a mesh independent solution within the region with the smallest cells, i.e., the second level of cell refinement regions.

The solver that is utilised in the present paper has been used also in the past by the same numerical group as in the present paper, for 2D-axisymmetric as well as 3D applications on droplet impact dynamics[14]. In these prior applications of the numerical solver, the conducted mesh independency studies indicated that for 2D-axisymmetric applications, the mesh independent solution can be considered when the computational cell size is 5 μm. For 3D cases, it has been seen that a computational domain with a cell size of 25 μm can be considered as the mesh independent solution, considering a balance of accuracy and computational cost. For all 3D simulations of the present manuscript, we went one level of refinement further utilising a cell size of 8 μm and 12.5 μm for the

computational domains of 100 μm and 150 μm gap, respectively, within the third level of refinement that corresponds to the region of the computational domain that the droplet expansion and infiltration takes place. This is the reason that a mesh independency study has not been conducted.

From a computational cost point of view, it would have been preferable to use an adaptive/dynamic mesh refinement. However, the customised version of the numerical solver that has been developed by the Authors in OpenFOAM v.2.2.1 is based on interFOAM and not interDyMFoam and therefore the dynamic mesh refinement has not been implemented yet to the solver. That is the reason that a local mesh refinement strategy using a static mesh with the appropriate cell size at the highest level of refinement has been followed instead of a dynamic mesh refinement strategy that refines/un-refines the mesh dynamically following the interface. For the future we are planning to implement a dynamic mesh refinement technique as this is necessary in order to reduce the significant computational cost of the present numerical simulations.

3. Results and Discussion

3.1 Model Validation with Experiments

The simulation results were compared against the experimental observations to validate the model for both water and ethanol droplet impacts. Figure 3 shows the experimental results from [13] of a 2.0 mm drop impacting a 150 μm gap at 1.5 m/s, in comparison with the corresponding numerical predictions. The simulation predicts the experiments well for both the extent of spread of the drop along the gap, i.e., the ½-width, w_p, and the height of the profile, h_p. Additionally, the simulation accurately predicts the time when the droplet cleaves and the liquid in the profile detaches from the drop on the surface of the gap, between 2 and 4 ms in Figure 3. The simulation predicts the phenomenon especially well up to approximately 3 ms when the profile and the droplet development are still within the region of the computational domain with the smallest cells (second level of mesh refinement in Figure 2). However, as can be seen at later times (4 ms and 5 ms), where parts of the droplet and the profile within the gap have exited from the finest mesh region, the numerical simulation prediction deviates from the experimental measurements. The coarse mesh region of the simulation is mesh dependent, so when the drop profile enters this region the simulation overpredicts the experimental measurements. For the purposes of this study, this deviation is allowable because we are interested in the period from the point of impact up to the point of cleaving, where the profile of the drop remains in the fine mesh region, the region of mesh independence.

As the profile detaches from the drop and travels further between the plates, a wave develops on the top of the profile—much more pronounced in the experimental results, Figure 3 at 4 and 5 ms. This is excess energy that needs to be dissipated from the cleaving event. Later photographs and longer simulations, both not shown, reveal that these waves eventually dissipate and both profiles minimize their surface area to resemble a semi-circle.

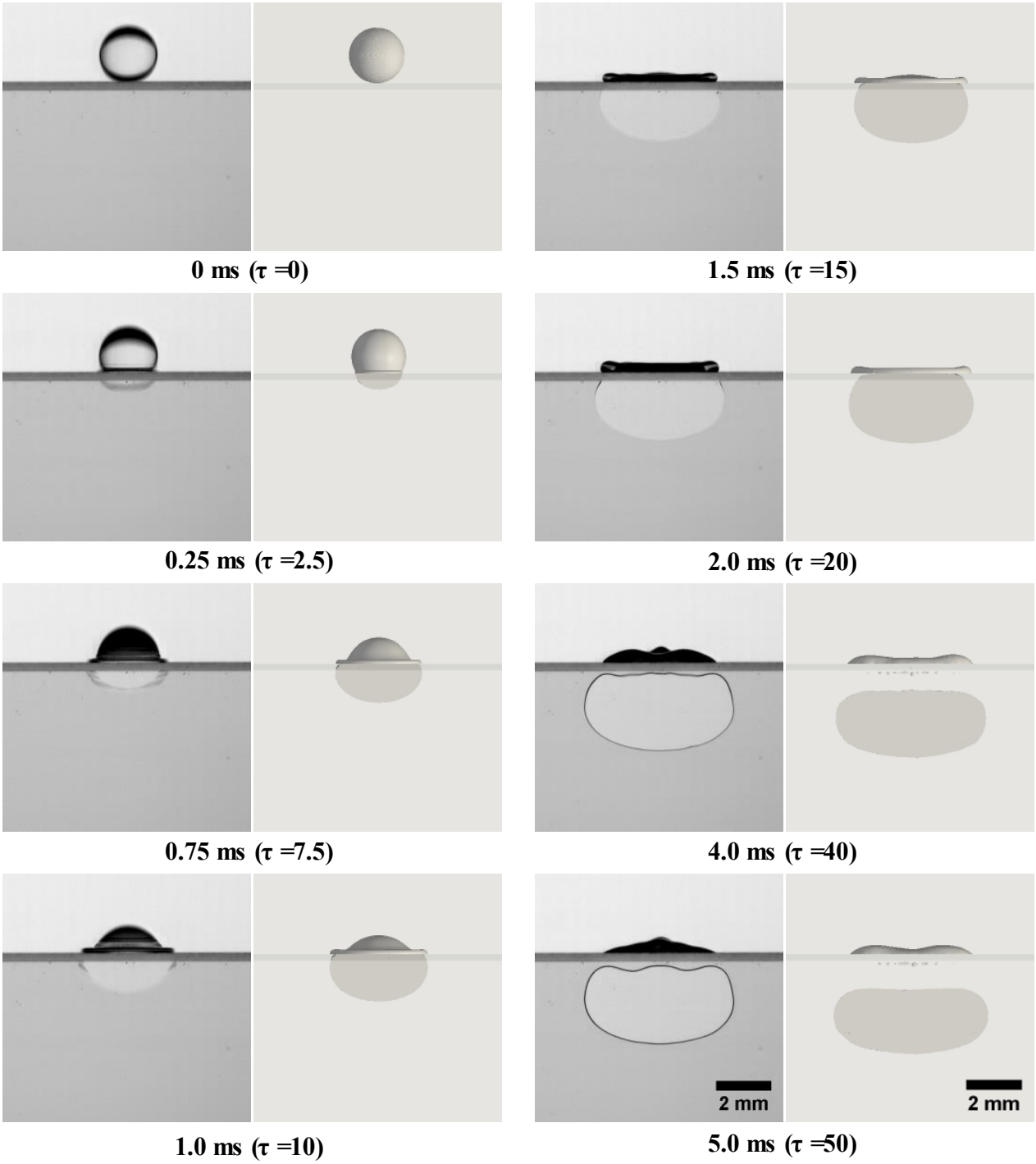

Figure 3. Comparison of experimental and numerical results for a 2.0 mm water drop impacting a 150 μm gap at 1.5 m/s. Dimensionless time, scaled by the impact velocity and gap width ($\tau = U_0 t/w$), is indicated in parentheses.

Figure 4 shows photographs of a 2.0 mm ethanol drop impacting a 100 μm gap at 0.9 m/s, in comparison with the corresponding numerical predictions. The simulation matches the experimental observations well for the spread of the ethanol drop over the gap as well as for the h_p and w_p of the ethanol profile within the gap. The model is also able to match when the ethanol drop cleaves and the ethanol on top of the gap separates from the ethanol within the gap, around 10 ms from the droplet impact in Figure 4. Similar to the modelled behaviour of the water profile in Figure 3, the ethanol profile is modelled to separate from the top of the gap at 15 ms in Figure 4, but to a much smaller extent than the water. This is due to the fact the ethanol profile within the gap has lower h_p values and

stays within the finest computational mesh region, and region of mesh independence, for almost the entire duration.

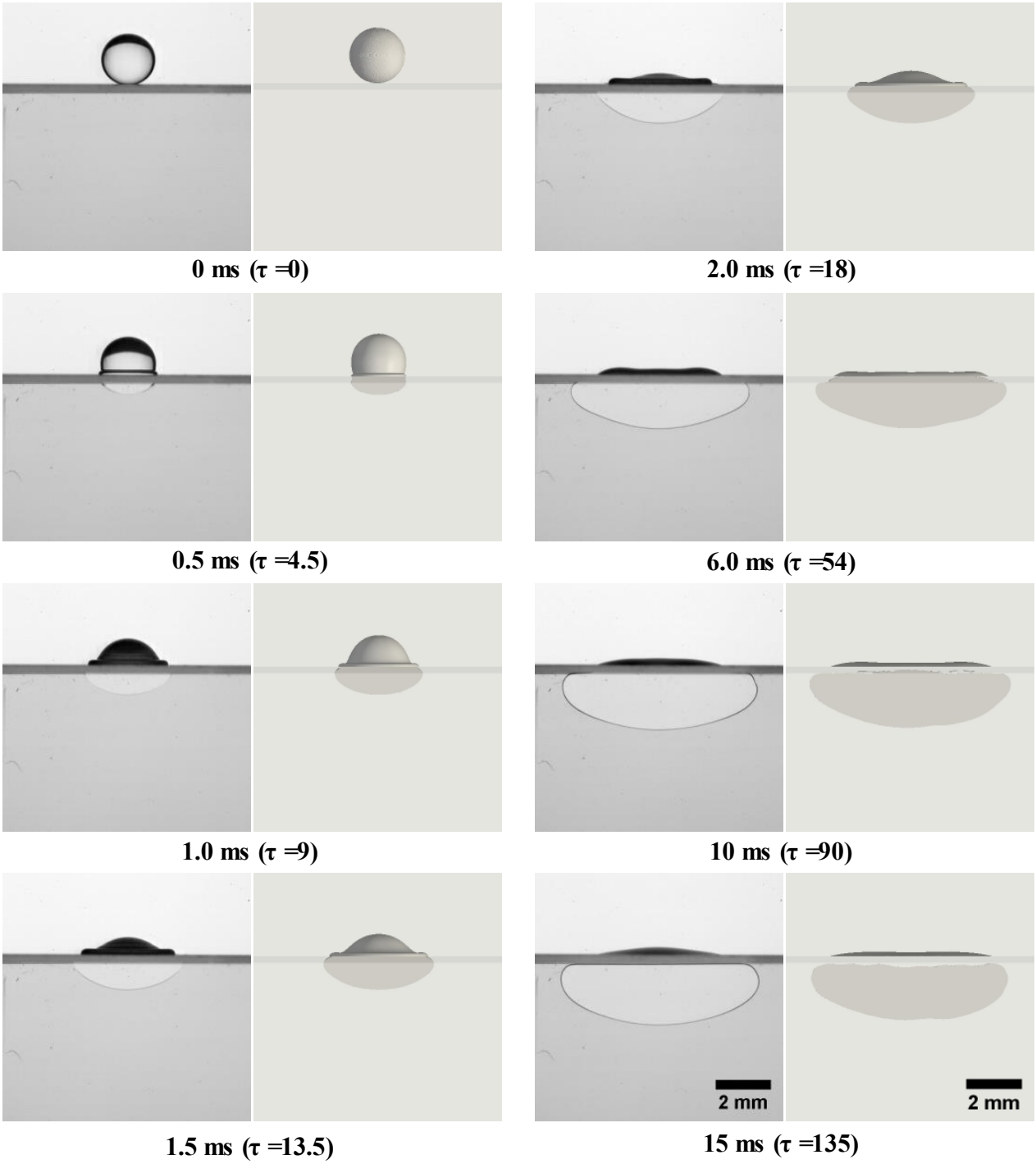

Figure 4. Comparison of experimental and numerical results for a 2.0 mm ethanol drop impacting a 100 μm gap at 0.9 m/s. Dimensionless time, scaled by the impact velocity and gap width ($\tau = U_0 t/w$), is indicated in parentheses.

The modelled profile growth, measured as the h_p and w_p of the profile, is compared against experimental measurements for four of the eight simulated cases in Figure 5. In each case the solid line is the modelled h_p and the dashed line is the w_p. Open diamonds and open circles represent the experimental h_p and w_p, respectively, with the error bars representing one standard deviation from the mean (N = 4). In all the simulated cases, the numerical model is in good agreement with the experiment measurements. As discussed earlier, the larger deviation in Figure 5b for the predicted height of the profile is an artifact of the simulation where the water profile exited the finer meshed

region and entered the coarser mesh region (mesh dependent region). From these results, it is concluded that the numerical simulation accurately describes a drop impacting and infiltrating into the narrow gap and that it can be used to further study this phenomenon, providing additional insight for the corresponding experimental measurements.

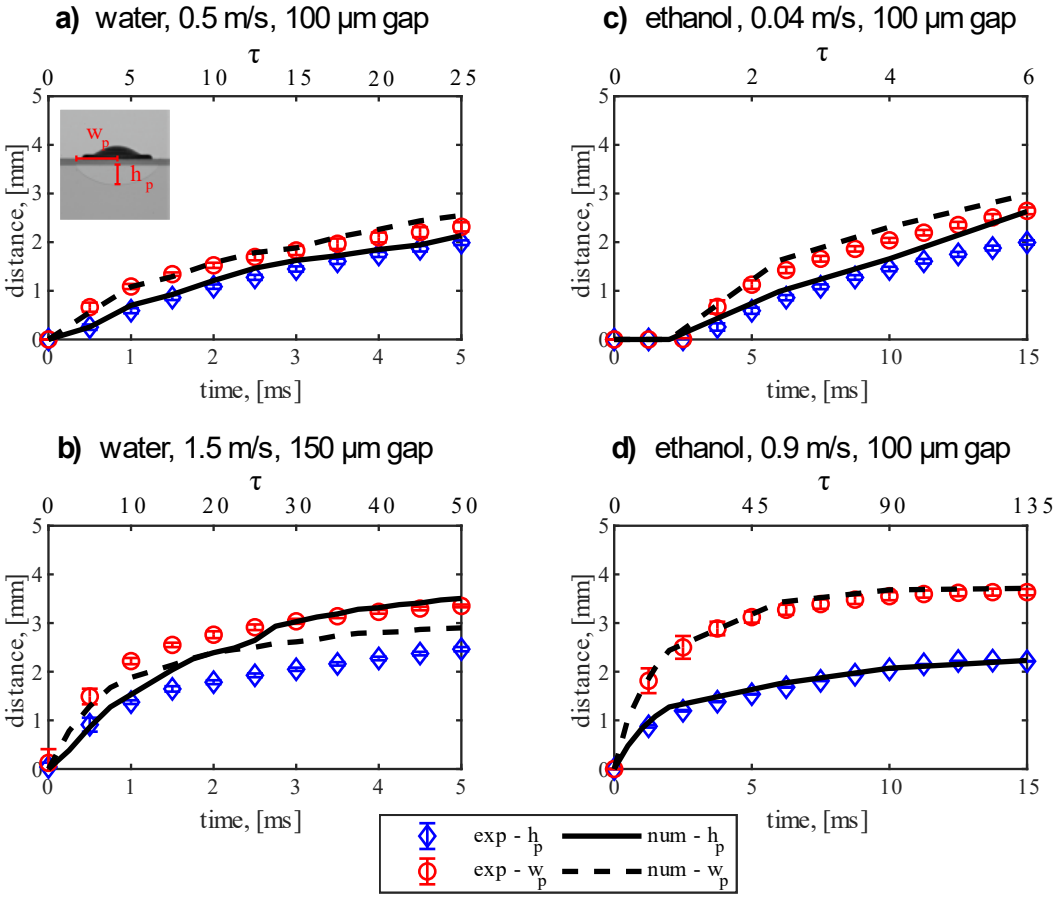

Figure 5. Comparison of experimental and numerical results for the liquid profile flow that develops in the narrow gap at four different conditions, each with a starting drop diameter of 2.0 mm. Fig. 5a is for water impacting a 100 µm gap at 0.5 m/s. Fig. 5b is for water impacting a 150 µm gap at 1.5 m/s. Fig. 5c is for ethanol impacting a 100 µm gap at 0.04 m/s. Fig. 5d is for ethanol impacting a 100 µm gap at 0.9 m/s. Time is indicated on the x-axis in both real time and dimensionless time, scaled by the impact velocity and gap width ($\tau = U_0 t/w$). The inset in Fig. 5a shows the referred to liquid profile height, h_p, and liquid profile ½-width, w_p. Error bars represent the standard deviation from the mean for the experimental results (N=4)

3.2 Infiltration behaviours of ethanol and water drops: experimental measurements.

Ethanol and water have similar viscosities, 1.35 cP and 1.0 cP at 20°C, respectively, but different surface tensions, 0.0215 N/m and 0.072 N/m, respectively. This is a difference of 35% between the viscosities and ~330% between the surface tensions. While water only cleaves at higher impact velocities, ethanol is observed to cleave at all the impact velocities tested—even when gently deposited at 0.04 m/s. Figure 6 shows this graphically as the dimensionless volume of liquid in the profile (made dimensionless by dividing by the initial volume of the drop) plotted against time scaled for inertia. For the low velocity impacts (We=7), the water fully infiltrates while the ethanol only achieves ~60% infiltration. The high impact velocity cases for water and ethanol (We=63) both cleave and achieve an approximate 35% infiltration.

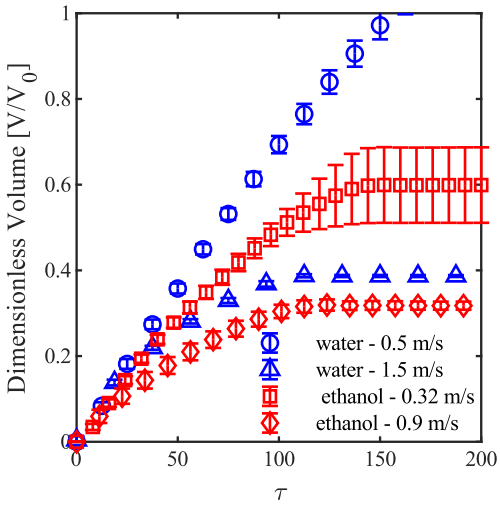

Figure 6. Comparison of the volume of water that infiltrates a 100 µm gap when it is impacted by a drop of water or ethanol at different velocities. The initial diameter of both drops is 2.0 ±0.04 mm, equal to a volume of 4.2 µl. While the water drop will completely infiltrate into the gap at low impact velocities and cleave at high impact velocities, ethanol will cleave at all impact velocities. Time is indicated on the x-axis in dimensionless time, scaled by the impact velocity and gap width ($\tau=U_0t/w$). Error bars represent one standard deviation from the mean (N=4).

One explanation for this behaviour is that ethanol spreads further and faster than water. Figure 7 shows a 2.0 mm ethanol (Figure 7a), and a 2.0 mm water drop (Figure 7b), impacting a 100 µm gap. The dimensionless time ($\tau=U_0t/D_0$) above the images of both drops has been scaled for inertia to remove the effect of the different impact velocities. The lower surface tension of ethanol means that the retraction force is smaller than that of water once the drop has reached its maximum spreading diameter. This factor produces a thinner drop for ethanol, comparing the drop heights at τ=2.5, in Figure 7. The liquid directly above the gap is the source of liquid for the flow infiltrating the gap. In the case of ethanol, this liquid source is depleted before the drop can retract and replenish the space above the gap, just as previously shown by Delbos [10] for water drop impacts on capillaries. This causes the drop to pin on both sides of the gap, leading to drop cleaving.

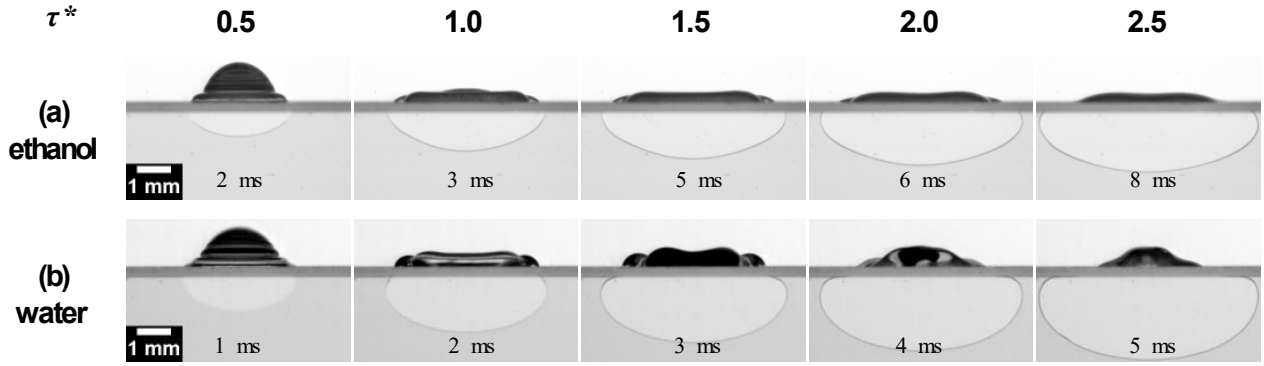

Figure 7. The droplet spread of 2.0 mm diameter ethanol drop impacting a 100 µm gap at 0.62 m/s (a) compared to the droplet spread of a 2.0 mm diameter water drop impacting the same gap at 1.0 m/s (b). The images are presented in dimensionless time to remove the effect of the different impacting velocities of the drops (for reader reference, real times are listed in the figure). Time has been made dimensionless using the impact velocity and the initial droplet diameter, $\tau^*=U_0t/D_0$. At times τ^*>1.0, the ethanol drop spreads further and recoils less than the water drop.

Another contribution that alters the dynamics between the water and ethanol droplet impacts might be the significantly different wettability characteristics along the bevel and within the gap for the two liquids (Figure 1). Figure 8 plots the dimensionless spreading factor, the lamella diameter divided by the initial diameter of the drop ($\beta = \frac{D}{D_0}$), of the 2.0 mm ethanol and water drop against

time scaled for inertia for three of the Weber numbers tested. In all three cases the ethanol spreads further, pins to a greater extent, and retracts less than the water. This is the same as what was simulated by Ding and Theofanous for liquids with low receding contact angles[11]. The result is less water above the gap for ethanol to act as a reservoir for the liquid flowing into the gap.

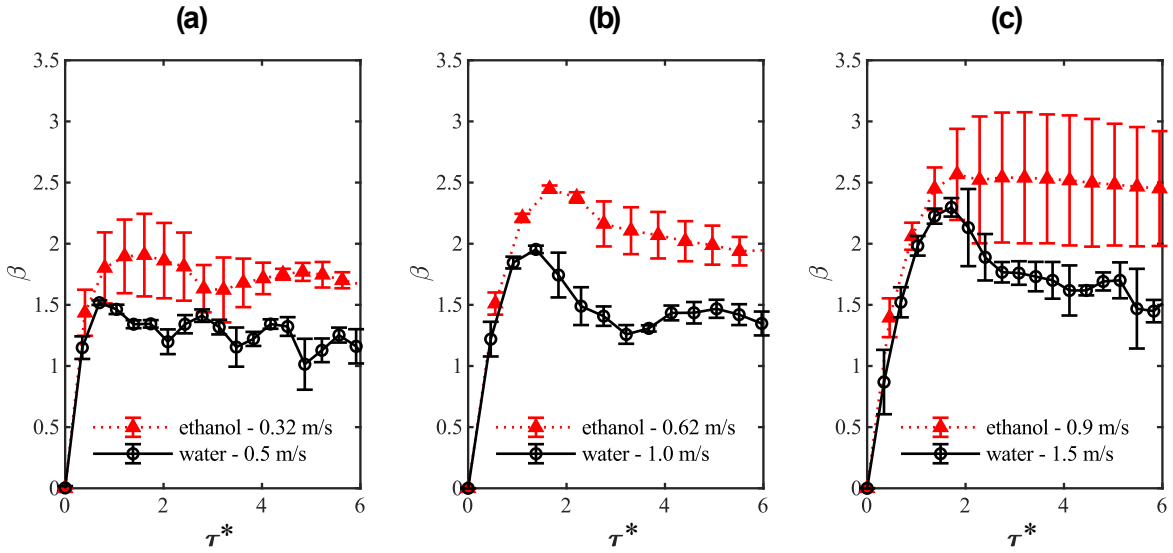

Figure 8. Comparison of dimensionless spread of an ethanol and water drop, both with initial diameter of 2.0 mm, on a 100 μm gap. Time on the x-axis is plotted in dimensionless time, $\tau^*=U_0t/D_0$. The Weber number in each part is the same for both liquids: (a) We=7, (b) We=28, (c) We=63. Ethanol spreads further than water because it has a lower surface tension. Error bars represent the standard deviation from the mean for the experimental results (N=4).

3.3 Infiltration behaviours of ethanol and water drops: numerical simulations

Figure 9 illustrates a 3D isometric view of the spatial and temporal evolution of the droplet impact for the case of a non-cleaving water droplet (Case 1 from Table 2) and the case of a cleaving ethanol droplet (Case 8 from Table 2). In both cases the water/air and ethanol/air interfaces are coloured by the velocity magnitude according to the provided colour legend. As can be observed, in the case of the non-cleaving water droplet the radially spreading droplet region maintains low velocity magnitude values with respect to the initial impact velocity. On the contrary, the central part of the droplet that is directly above the gap and constitutes the feeding part of the liquid that penetrates the gap shows higher velocities than the initial impact velocity. It is quite interesting that exactly the opposite happens for the cleaving ethanol droplet impact. As the ethanol drop spreads, the radially spreading region shows higher velocity values than the initial impact velocity while the central part shows much lower velocity values. It is also characteristic that, as also observed in the experiments (Figure 7), the ethanol droplet spreads to a greater extent than the water droplet.

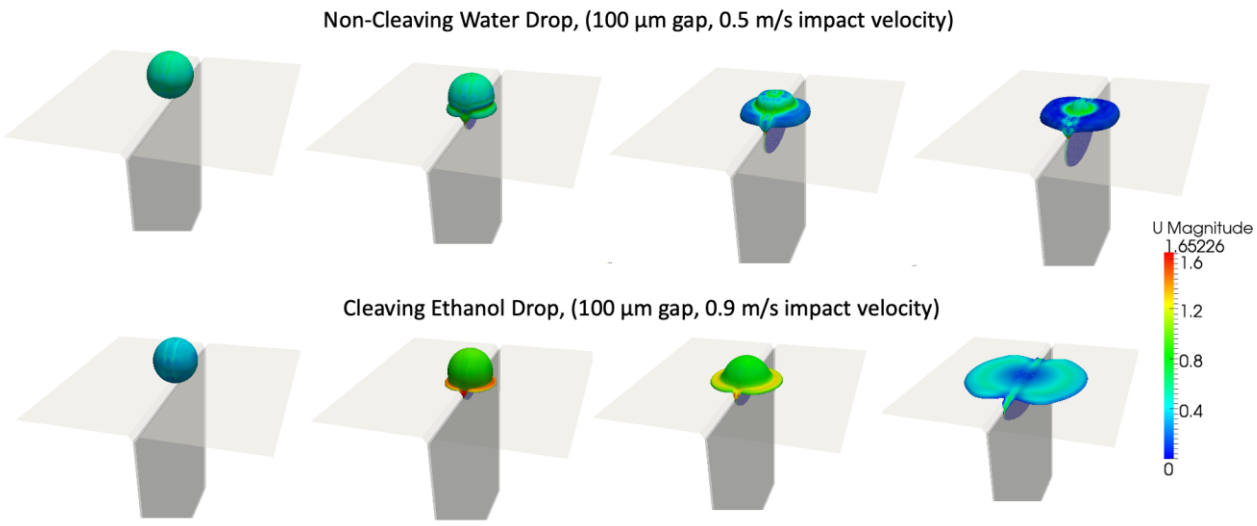

Figure 9. Comparison between non-cleaving water and cleaving ethanol drops through the temporal and spatial evolution of the water/air interface coloured by the velocity magnitude.

Figures 10 and 11, show the evolution of the resulting pressure (a) as well as the resulting vertical velocity component (b) in the case of a non-cleaving water drop (Figure 10, Case 1) and a cleaving ethanol drop (Figure 11, Case 7), respectively. In both cases, for each time instance, the colour scale spans between the maximum and minimum values of the absolute pressure [Pa] and the vertical velocity component [m/s], respectively. Also, the absolute pressure and vertical velocity component are plotted for the two liquids and the surrounding air—a continuous line demarks the interface between the liquid and the air. In the non-cleaving water case two high-pressure stagnation regions are initially formed in the vicinity of the top corners of the bevel that then gradually grow and merge into a much wider high-pressure region on top of the gap that extends up to the spreading droplet borders. Some, low pressure regions are traced locally, at interface inflection points. Examining the vertical velocity component distribution for the same time instances, it is evident that the wider high-pressure region creates a path of continuous downward liquid movement that enters into the gap through the bevel. Therefore, for the non-cleaving water droplet there is a continuous feed of liquid into the gap through the bevel region. It should be highlighted here that this behaviour was observed in all the simulated water droplet impacts (cases 1-4 from Table 2).

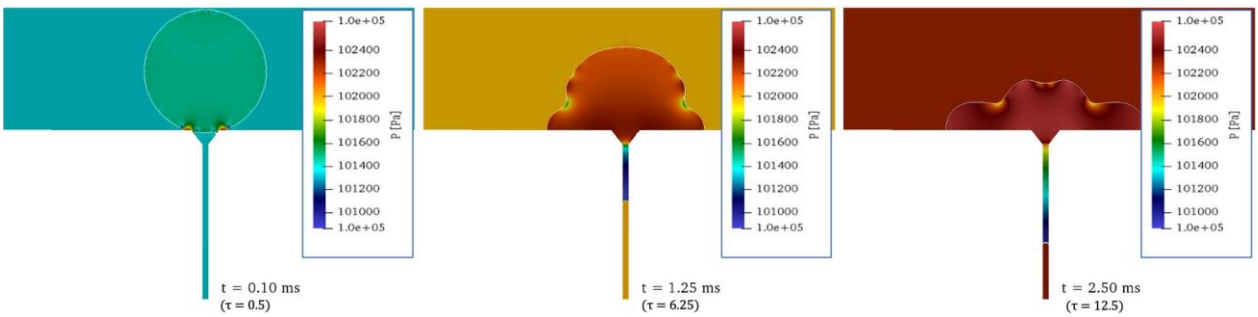

(a)

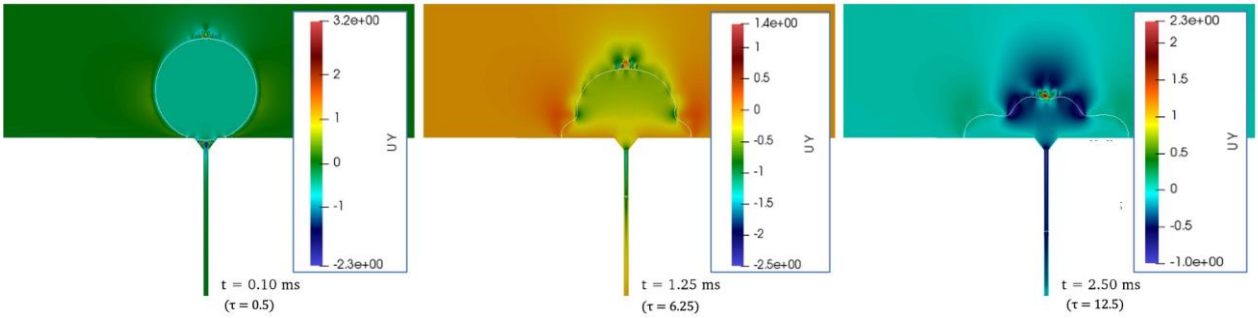

(b)

Figure 10. Pressure (a) and vertical velocity component (b) distribution in a central vertical plane for a non-cleaving water drop impacting a 100 μm gap at 0.5 m/s. Dimensionless time, scaled by the impact velocity and gap width ($\tau = U_0 t/w$) is indicated in parentheses.

For the cleaving ethanol case (Figure 11), a wider, uniform, high-pressure region within the bevel and the surrounding liquid region is observed at the beginning that gradually attenuates leaving just two narrow high-pressure stagnation regions close to the top-corners of the bevel (a). This "opposite" behaviour of the pressure field within the ethanol droplet in comparison to the water droplet, results in an interruption of the vertical pathway that feeds the gap with liquid. This is more obvious from the gradually developing zero vertical velocity component zone on top of the bevel (b). It should be also highlighted here that the same behaviour was observed in all of the simulated ethanol droplet impacts (cases 5-6 from Table 2).

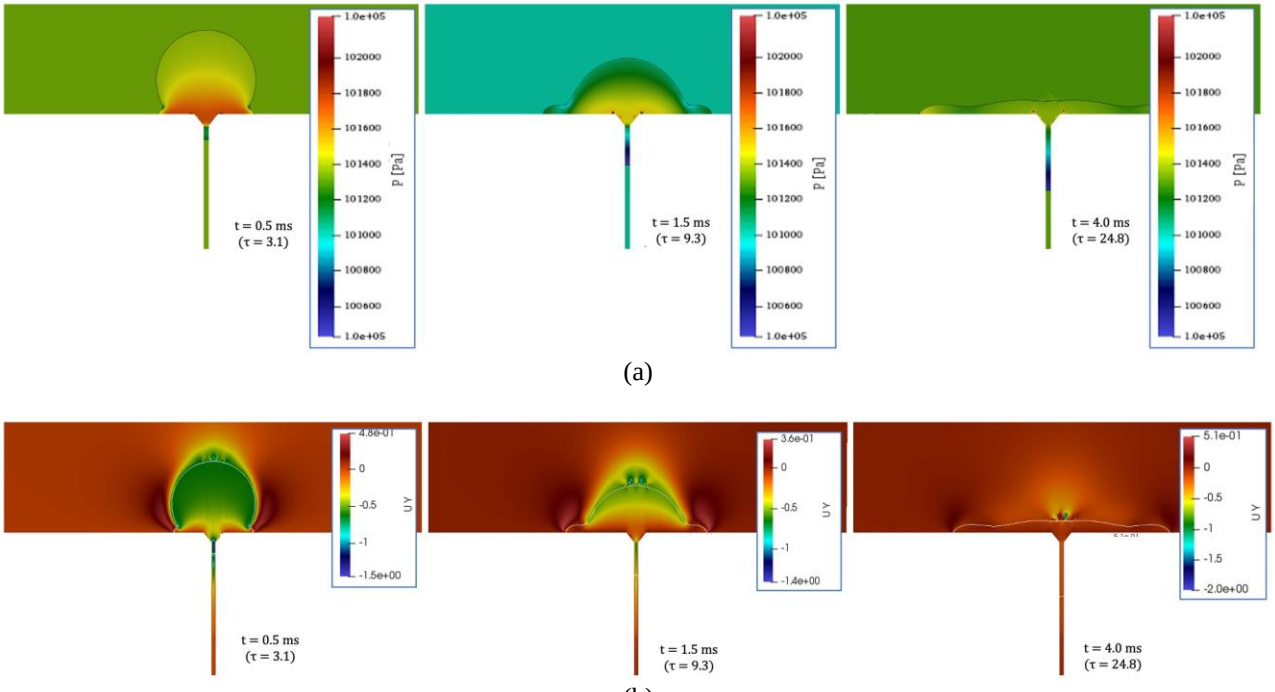

(a)

(b)

Figure 11. Pressure (a) and vertical velocity component (b) distribution in a central vertical plane for a cleaving ethanol drop impacting a 100 μm gap at 0.62 m/s. Dimensionless time, scaled by the impact velocity and gap width ($\tau = U_0 t/w$) is indicated in parentheses.

From the above comparison, it is evident that the liquid movement within the bevel region is different between the water and ethanol droplet impacts. To better quantify the difference in the droplet dynamics between a water (Case 1 from Table 2) and an ethanol case (Case 7 from Table 2), the horizontal velocity component along the central axis that passes through the bevel has been plotted for similar dimensionless times, τ, Figure 12. The horizontal velocity component is in both cases normalised by the impact velocity, and the horizontal distance has been normalized by the total gap

length, L^*. As can be observed for the water impact, the fluid that moves along the groove decelerates. The peak velocity is progressively decreasing from 3.8 times (τ = 3) to 1.0 time (τ = 15.75) and 0.8 times (τ = 33.75) the impact velocity value, respectively. However, in the ethanol case it initially decelerates, reducing from 3.6 times (τ = 3.1) to 1.2 times (τ = 15.5) and then accelerates increasing from 1.2 times (τ = 15.5) to 2.0 times (τ = 34.1) the impact velocity value.

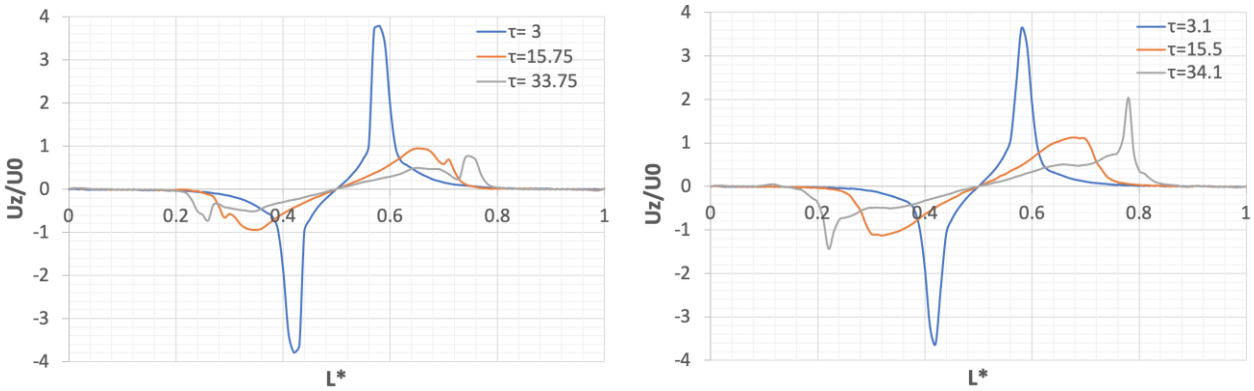

(a) (b)

Figure 12. The droplet spread of 2.0 mm diameter water drop impacting a 100 µm gap at 1.5 m/s (a), compared to the droplet spread of a 2.0 mm diameter ethanol drop impacting the same gap at 0.62 m/s (b). L^* is the horizontal distance of the drop rim normalised by the length of the bevel. Dimensionless time is time scaled by the impact velocity and gap width ($\tau = U_0 t/w$).

The difference in surface tension forces between the water and ethanol droplets has a significant effect in the resulting liquid dynamics within the portion of the drop that is spreading, and this contributes to the cleaving/non-cleaving outcome. Due to the lower surface tension of ethanol, the liquid above the gap primarily is dragged in the radial direction shortly after impact. This results in a much higher radial force in comparison to the vertical force within the gap, which is maintained only by capillary action at this stage. As a result, the portion of the drop directly above the gap continuously thins and the drop eventually cleaves because there is insufficient liquid available to feed into the gap.

Figure 13 compares the dimensionless volume of liquid (V/V_0) that spreads on top of the plates against the dimensionless volume of liquid that penetrates the narrow gap with respect to dimensionless time for Cases 2 (water droplet) and 7 (ethanol droplet) from Table 2 (the initial volume of the drop, V_0, is used in both cases to make the volume dimensionless). The inset within Figure 13 shows the two planes beyond which the liquid volume was measured. Specifically, the volume of liquid in the bevel and one half of the drop lamella spread is omitted from Figure 13. The gradients of the resulting curves represent the corresponding liquid spreading and penetration flow rates. The water penetration rate is always greater than ethanol's penetration rate, while ethanol's spreading rate is always greater than water's spreading rate. Additionally, the water penetration flow rate into the gap is significantly higher than the radially spreading flow rate. However, in the case of ethanol the corresponding difference is much lower.

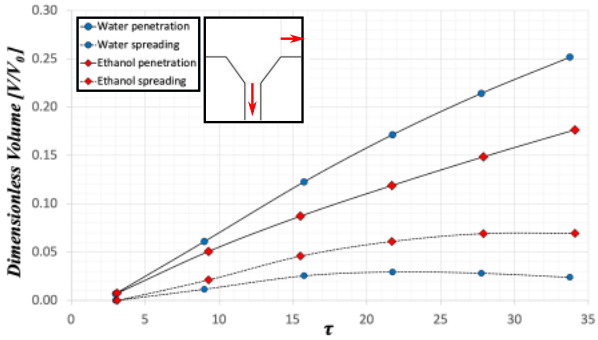

Figure 13. Dimensionless volume of liquid (V/V_0) spreading onto the horizontal plates (to the right and left of the bevel) with respect to dimensionless time (τ) and dimensionless volume of liquid penetrating into the narrow gap (in between the vertical plates and below the bevel) with respect to dimensionless time ($\tau=U_0t/w$). The water drop impacts a 100 μm gap with an impact velocity U_0 of 1.5 m/s while the ethanol drop impacts a 100 μm gap with an impact velocity U_0 of 0.62 m/s. The inset shows the planes beyond which the liquid volume was measured.

Summarising, all the above qualitative and quantitative results from the numerical simulations further justify the speculation from the experimental observations that the resulting flow behaviour is mainly attributed to the difference in the surface tension coefficient between ethanol and water. It is evident that the effect of surface tension is quite significant in such droplet impact and penetration phenomena because it completely alters the liquid flow field within the droplet boundaries both in the radial spreading direction as well as in the vertical direction into the gap. This alteration results in a high radial flow rate that is comparable to the vertical flow rate. In other words, as the difference between the vertical and radial flow rate decreases, drops will tend to cleave. This further explains the fact that water droplets tend to cleave only for high impact velocities where the difference between the penetrating and radically spreading flow rates significantly decreases as the penetrating flow rate remains at the same order while the corresponding spreading flow rate significantly increases in agreement with previous investigations that are cited in the introductory section of the present investigation.

3.4 Advancing Contact Angle of Infiltrating Liquid

In an earlier paper by two of the present authors[13], an assumption was made regarding the contact angle at the leading edge of the profile that is penetrating into the gap. The assumption was that for the first 0.5 ms after impact the contact angle was greater than 85 degrees, and then relaxed to a constant advancing contact angle of 37 degrees for times t>1.5 ms after impact [13]. Using the numerical simulation of the present investigation, we took a section perpendicular to the gap to graphically measure the advancing contact angle of the profile immediately after impact. Figure 14 shows the apparent advancing contact angle of a 2.0 mm water drop impacting a 150 μm gap at 1.5 m/s. In the first few instances following the impact water is forced into the gap and the water at the centre of the gap is traveling at a velocity twice that of the impact velocity. Here, the contact angle is ~90 degrees. The contact angle oscillates until t=0.5 ms and is still in excess of 70 degrees by 1.0 m/s. These measurements support the assumption of a high initial advancing contact angle for times immediately after impact. For t>0.3ms, the graphically measured contact angles are in good agreement with the correlation proposed by Jiang et al. [19], which adjusts the contact angle based on the velocity of the contact line. Table 3 presents the calculated dynamic contact angle for several contact line velocities. The initial shock of impact and subsequent oscillations make this correlation less accurate for t<0.3 ms after impact.

However, a major shortcoming of adjusting the advancing contact angle for predictive modelling is accurately determining the velocity of the contact line. An example of this can be seen in Figure 14

at 0.15 ms. Here, the velocity of the water at the mid-point in the gap is ~3 m/s and the velocity of the fluid near the gap's edges is ~1 m/s. The fluid interface in the gap is clearly convex, which would require a contact angle of >90° and a contact line velocity >3 m/s according to the correlation proposed by Jiang et al. [19]. This is three times higher than the near wall velocity indicated by the simulation.

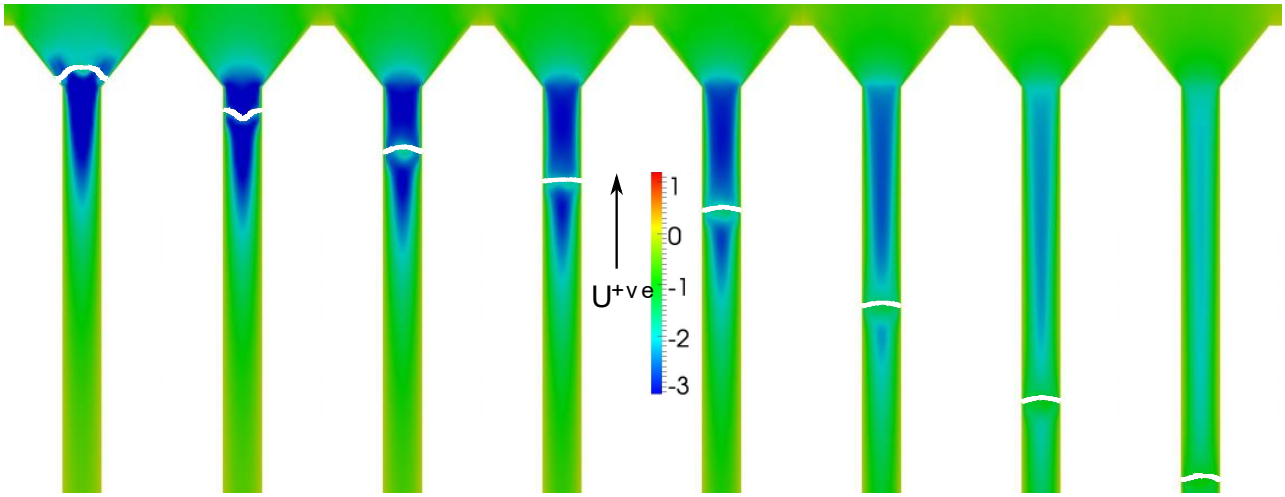

Figure 14. Model results for the relaxation of the apparent advancing contact angle for a 2.0 mm water droplet impacting a 150 µm gap at 1.5 m/s. The thick white line denotes the location of the advancing air-water interface, and the coloured contours indicate the vertical velocity component of the water and air above and below the interface, respectively. The contact angles were graphically measured in ImageJ[20]. Dimensionless time is time scaled by the impact velocity and drop diameter ($\tau^*=U_0t/D_0$).

Table 3. Adjusted contact angles based on the velocity of the contact line from the dynamic contact angle correlation proposed by Jiang et al. [19]. The advancing contact angle used in the correlation proposed by Jiang et al. [19] is 36 degrees.

U_{CL} [m/s]	0.1	0.5	1	1.5	2	2.5	3
Θ_d	44°	57°	68°	76°	83°	86°	94°

The high contact angles immediately after impact do relax in a short period of time to values typically measured by standard contact angle measurement techniques. The advancing contact angle of the profile was graphically measured for the water drop impacting the 100 µm and 150 µm gap at 0.5 m/s. Measurements were taken at 2, 3, and 4 ms after impact (τ*=0.5, 0.75, and 1, respectively). The average advancing contact angle for the profile was 33.7 degrees for the 100 µm gap and 28.5 degrees for the 150 µm gap. These angles are between the advancing and receding contact angles previously measured for this liquid-solid system (Θ_A = 37°, Θ_R = 8° [13]). Therefore, caution should be used when assuming contact angles within capillaries after a drop impact for times less than τ*=1.0.

Another interesting observation is the "kink" in the interface at 0.15 ms in Figure 14. We speculate that the kink formation is a result of the inertia of the impacting drop. When the drop first enters the capillary, it must decelerate to velocity that would develop solely under capillary pressure. In Figure 14, the inertia of the liquid in the capillary is great enough to increase the advancing contact angle to 90, but it is not great enough to overcome the surface tension of water to break away and form individual droplets. A similar phenomenon occurs when a drop impacts a cylinder at some velocity and the pendent drop that forms on the opposite side is on the verge of detachment due to insufficient inertia[21,22].

4. Conclusions

The present paper further explores the physics of drop impact onto a narrow rectangular gap, to offer deeper insights about the process of drop infiltration and imbibition originally observed in our earlier study. Experiments have been performed using water and ethanol, which have very different behavior especially in terms of drop cleaving after the impact. A customized, advanced numerical VOF code, based on the OpenFOAM platform, has been used to reproduce the experimental results and to investigate the physical reasons about cleaving, radial and vertical flows.
The main findings can be stated as:
1) Water drops only cleave at high impact velocities, while ethanol drops cleave at all impact velocities, even when gently deposited at 0.04 m/s.
2) This behaviour is driven by the lower surface tension of ethanol, which causes ethanol to spread faster than water. Furthermore, the lower surface tension of ethanol means that the retraction force is smaller than that of water once the drop has reached its maximum spreading diameter. This factor produces a thinner lamella for ethanol and, since the liquid directly above the gap is the source of liquid for the flow infiltrating the gap, results in the drop cleaving. This specific behaviour does not depend on surface wettability, at least for the two considered fluids.
3) For cleaving water drops, the central part of the drop directly above the gap shows higher vertical velocities than the initial impact velocity. The opposite happens for the cleaving ethanol drops, for which the central part shows lower vertical velocities than the initial impact velocity. This is again linked to the fact that the liquid above the gap flows faster in the radial direction for ethanol, stopping the vertical liquid feed into the gap.
4) The qualitative and quantitative analysis of the experimental investigations revealed that the difference in surface tension between the two examined liquids is responsible for a complete alteration of the resulting transient flow field within the droplet boundaries in each case. As the difference between the penetration flow rate and the spreading flow rate narrows, cleaving becomes more likely.
5) Small deviations between numerical simulations and experimental data appear after a given time of the spreading, due to the fact that, to avoid extremely long computational times, the regions interested by the fluid flow after a time lag, have coarser cell sizes. This confirms the need of very small grid cells, about 2 microns, for very accurate simulations of drop impact. Additionally, advanced VOF simulations are indeed able to reproduce this kind of physical processes with very high fidelity. Advanced VOF solver constitutes a valuable tool for further quantifying and explaining experimental observation and potentially expanding experimental databases for future investigations.
6) Caution should be used when assuming contact angles within a capillary immediately after a drop impact. In these experiments typical contact angle values were generally measured only at times when $\tau^*>1.0$.

Finally, a liquid with a lower surface tension would generate a lower capillary pressure. Therefore, it would be reasonable to assume that for the same impact Weber number, a lower surface tension liquid would have greater infiltration into a gap. It is shown that at low Weber numbers this is not the case: lower surface tension liquids will infiltrate less and cleave more easily than higher surface tension liquids. Therefore, use of surfactants, for example, may not be optimal if absorption of liquid sprays in porous material is preferred in an actual application with a fluid impingement. This also means that the Weber number alone is not able to offer a good, general prevision about the drop impact onto narrow gaps or pores. Further studies are required that cover a range of droplet diameters and surface tensions to construct a general model to predict the penetration and cleaving behavior of drops on narrow gaps or pores.

Nomenclature

C_a	capillary number - $Ca = \frac{\mu U_{CL}}{\gamma}$
CI	confidence interval
D_0	initial droplet diameter
F_s	surface tension force
f_{Hoff}	Hoffman function
h_p	height of liquid profile
L*	dimensionless length - $L^* = \frac{L}{D_0}$
N	number of samples
p	pressure
t	time
U	velocity
U_0	impact velocity
U_{CL}	contact line velocity
V_{liquid}	volume of liquid
V_0	initial volume of drop
VOF	Volume Of Fluid
w	gap width
We	Weber number $We = \frac{\rho U_0^2 D_0}{\gamma}$
w_p	liquid profile ½-width
Greek letters	
α	volume fraction of liquid phase
$\tilde{\alpha}$	smoothed volume fraction
β	dimensionless spread factor, $\beta = \frac{D}{D_0}$
γ	surface tension coefficient
θ_d	dynamic contact angle
θ_ε	equilibrium contact angle
θ_A	advancing contact angle
θ_R	receding contact angle
κ	interface curvature
μ	viscosity
μ_b	bulk viscosity
μ_g	gas phase viscosity
μ_l	liquid phase viscosity
ρ	density
ρ_b	bulk density
ρ_g	gas phase density
ρ_l	liquid phase density
τ	dimensionless time scaled for gap spacing, $\tau = \frac{U_0 t}{w}$
τ*	dimensionless inertia time, $\tau^* = \frac{U_0 t}{D_0}$

Acknowledgments

We would like to acknowledge and thank Joanna Kolodko, a summer undergraduate research student at the University of Toronto, for her contribution in conducting some of ethanol droplet experiments. Dr. Manolia Andredaki, Dr. Anastasios Georgoulas and Prof. Marco Marengo would like to acknowledge the financial support from the European Space Agency (ESA CORA-MAP projects WHISKIES, TOPDESS and ENCOM4). Prof. Sanjeev Chandra and Dr. D. Jordan Bouchard would like to acknowledge financial support from the Natural Sciences and Engineering Council of Canada.

Conflict of Interests
No conflict of interests declared

Availability of data and material
The data that support the findings of this study are available from the corresponding author upon reasonable request.

Author's contributions
All authors contributed to the study conception and design. Experiments were performed and processed by D. J. Bouchard; numerical simulations were performed by M. Andredaki, and A. Georgoulas. Analysis and interpretation of the data was performed by all authors. The first draft of the manuscript was written by D. J. Bouchard, M. Andredaki, and A. Georgoulas. All the authors commented on subsequent versions of the manuscript and approved the final manuscript.

References
[1] C. Josserand and S.T. Thoroddsen, Annu. Rev. Fluid Mech. **48**, 365 (2016).

[2] A.L. Yarin, Annu. Rev. Fluid Mech. **38**, 159 (2006).

[3] D. van der Meer, Annu. Rev. Fluid Mech. **49**, 463 (2016).

[4] T. Gambaryan-Roisman, Curr. Opin. Colloid Interface Sci. **19**, 320 (2014).

[5] G. Liang and I. Mudawar, Int. J. Heat Mass Transf. **106**, 103 (2017).

[6] J.B. Lee, A.I. Radu, P. Vontobel, D. Derome, and J. Carmeliet, J. Colloid Interface Sci. **471**, 59 (2016).

[7] J.B. Lee, D. Derome, and J. Carmeliet, J. Colloid Interface Sci. **469**, 147 (2016).

[8] N.C. Reis, R.F. Griffiths, M.D. Mantle, and L.F. Gladden, Int. J. Heat Mass Transf. **46**, 1279 (2003).

[9] I. V. Roisman, A.N. Lembach, and C. Tropea, Adv. Colloid Interface Sci. **222**, 615 (2015).

[10] A. Delbos, E. Lorenceau, and O. Pitois, J. Colloid Interface Sci. **341**, 171 (2010).

[11] H. Ding and T.G. Theofanous, J. Fluid Mech. **691**, 546 (2012).

[12] M. Andredaki, A. Georgoulas, and M. Marengo, Phys. Fluids **32**, (2020).

[13] D.J. Bouchard and S. Chandra, Phys. Fluids **31**, 13 (2019).

[14] K. Vontas, C. Boscariol, M. Andredaki, A. Georgoulas, C. Crua, J.H. Walther, and M. Marengo, Fluids **5**, 1 (2020).

[15] J. Brackbill, D. Kothe, and C. Zemach, J. Comput. Phys. **100**, 335 (1992).

[16] A. Georgoulas, P. Koukouvinis, M. Gavaises, and M. Marengo, Int. J. Multiph. Flow **74**, 59 (2015).

[17] The OpenFOAM Foundation, (2021).

[18] S.F. Kistler, in *Wettability*, edited by J.G. Berg (Marcel Dekker, Inc, New York, 1993), pp. 311–429.

[19] T.-S. Jiang, O.H. Soo-Gun, and J.C. Slattery, J. Colloid Interface Sci. **69**, 74 (1979).

[20] C.A. Schneider, W.S. Rasband, and K.W. Eliceiri, Nat. Methods **9**, 671 (2012).

[21] K. Piroird, C. Clanet, É. Lorenceau, and D. Quéré, J. Colloid Interface Sci. **334**, 70 (2009).

[22] M. Safavi and S.S. Nourazar, Int. J. Multiph. Flow (2018).